Nanotubes of core/shell Cu/Cu_2O as anode materials for Li-ion rechargeable batteries.

Maksudul Hasan, Tamjid Chowdhury and James F. Rohan*

Tyndall National Institute, University College Cork, Lee Maltings, Cork, Ireland.

* Corresponding author. Tel.: +353 21 4904224; fax: +353 21 4270271.

E-mail address: james.rohan@tyndall.ie (James F. Rohan)

Abstract.

A direct electrodeposition technique for Cu nanotube array fabrication and subsequent conversion of the deposited Cu into Cu_2O has been developed. The Cu_2O nanotube arrays have shown high capacity, cyclability and rate capability. The cycling performance of the Cu_2O nanotubes show a high level of structural integrity with capacity retention even after 94 cycles when cycled at 1C to 3C rates. The enhanced electrochemical performance of the Cu_2O nanotubes comes from high surface area, electrolyte access, high electrical conductivity of Cu core support and structural integrity of the oxide shell active material.

Introduction

One dimensional (1D) nanostructures have recently attracted much attention for potential applications in nanoscale energy storage/conversion devices [1-3] due to their unique physical properties that differ from the bulk materials. 1D nanostructures provide additional electrode surface area, to facilitate Li^+ insertion/extraction and short path lengths for electronic and Li^+ transport and thus the possibility of higher charge/discharge rates [4]. Recently, metal oxides of Fe, Co and Cu have been described as anode materials for Li-ion batteries based on a novel reaction mechanism proposed by Tarascon et al [5]. More recently, they demonstrated the idea of the so called "conversion reactions" for 1D Fe_3O_4 nanorod structures [6]. The reaction mechanism involves the compositional transformation of metal oxides to metal nanodomains dispersed in Li_2O during the charging process which regain the original composition during the discharge process. The reaction mechanism differs from the classical Li^+ insertion/de-insertion. High rate capability (for example, 80% capacity retention at 8 C rates) was reported [6] using these nanorod arrays. Mesoporous Co_3O_4 nanorods of the same "conversion reactions" family have been synthesised by an ammonia-evaporation-induced method on Si wafer, glass slide, Cu or Ti foil, and polystyrene substrates [7]. This template-free method permits the growth of large area nanorod arrays on various substrates. Cu_2O is also a "conversion reaction" oxide family member with demonstrated high capacity [8]. Cu_2O nanowires have been fabricated in anodised alumina oxide (AAO) templates by electrodeposition from a copper acetate/lactate bath with Cu as co-deposit [9]. The variation of local pH at the electrode surface during the deposition process results in the spontaneous potential oscillation and a Cu/Cu_2O composite deposit. However, the low efficiency of the bath has restricted its applications. Yang et al. oxidised Cu_2S nanowires under O_2 at elevated

temperature and observed the formation of polycrystalline nanowires containing both Cu and Cu_2O [10].

In this paper, we will report a novel fabrication route to Cu nanotubes based on the direct electrodeposition of Cu in the pores of an alumina template from an additive containing $CuSO_4$ bath and the controlled conversion of the deposited Cu into Cu_2O. The novelty of the method is the simplicity and control in producing a very high quality Cu/Cu_2O nanotube array. Cu nanotubes have been grown previously in polycarbonate templates through a chemical reduction method for use as additives in the negative electrode of Ni-MH batteries [11]. Another method involved sequential high temperature processing steps to achieve template assisted nanotube deposition [12]. We will present the mechanism for Cu nanotube growth and conversion to Cu_2O for use as a lithium battery anode. Characterisation of the materials by XRD, electrochemical performance and microstructure analysis by SEM is utilised to correlate with the Li cycling performance.

Experimental

Cu nanotubes were electrodeposited in AAO (Anodisc membranes, Whatman, 19.5 mm in diameter excluding of the polypropylene supporting ring, 60 μm thick and 10^9 pores per cm^2). The pore diameter was 250 to 300 nm. The complete fabrication process of Cu_2O nanotubes is illustrated in Fig. 1. A 500 nm thin layer of Ni conducting layer was deposited onto one side of AAO template by e-beam evaporation (Temescal FC-2000). The electrodeposition was carried out in a 0.24 M $CuSO_4$ (Fisher Scientific analytical reagent grade) and 1.8 M H_2SO_4 (Air products 96%) bath at room temperature with slow

stirring of the solution. The additives used in the bath were polyethylene glycol (PEG) (300 ppm) (SigmaUltra, mol. wt. 3350, powder) and Cl^- (50 ppm) as NaCl (BDH, analytical reagent grade). A constant current 40 mA was applied for Cu nanotubes electrodeposition using a potentiostat CH Instruments 660C in a two electrode set up with Cu foil as the anode and the Ni substrate at the base of the pores of the AAO as the cathode. The AAO template was mounted vertically in the cell facing the anode with the Ni seed layer on the opposite side open to the solution. The spacing between the anode and cathode was maintained at 1 cm. A Cu wire was connected to the Ni conducting side of the template by Ag conductive paint (Radionics Ltd. Ireland). The deposition rate was approximately 0.22 μm per minute. After Cu deposition the aluminium oxide template was dissolved in 0.75 M NaOH (Sigma Aldrich) solution for 50 min, washed with DI water and dried in air.

The electrodeposited Cu was converted to Cu_2O by oxygen plasma treatment (March Plasmod GCM 200) at 250 watts. The Li capacity test of Cu_2O nanotubes was performed by cyclic voltammetry and constant current experiments using a CH Instruments 660C potentiostat and a three electrode set-up. The active weight of the of Cu_2O nanotubes was estimated from the height, diameter (calculated from conversion rate plots in the results section for Cu to Cu_2O) and number of nanowires (10^9 pores/cm^2 in Whatman AAO membranes) in a 19.5 cm^2 AAO template, and assuming the Cu_2O density of 6.09 g/cm^3, The Cu_2O nanotubes arrays as obtained were mounted vertically in a Pyrex glass cell filled with electrolyte, in which Cu_2O nanotubes assembly was served as working electrode and 0.25 mm lithium foil (Sigma-Aldrich) as counter and reference electrodes. The electrolyte was 1M $LiPF_6$ in ethylene carbonate (EC)/diethyl carbonate (DEC) (1:1, in volume) (Sigma-Aldrich). Lithium foil of 0.25 mm thickness (Sigma-Aldrich) served

as counter and reference electrodes. The cell was assembled in an MBraun argon-filled glove box where O_2 and H_2O were maintained at or leow a 0.1 ppm level. The capacity values were measured by calculating the total Coulombic charge during Li^+ ions insertion and extraction for the discharge and charge curves, respectively.

The materials were characterised by X-ray powder diffraction (Phillips PW3710-MPD with Cu Kα radiation, l = 1.54056 Å, at 40 kV (35 mA) and data was analysed using Philips X'pert XRD software). The deposit microstructure was analysed by scanning electron microscopy (SEM) (FEI Nova 630 Nano-SEM at 15 kV).

Results and Discussion

Well ordered and homogeneous Cu nanotubes were obtained using a template mediated electrodeposition technique from a $CuSO_4/H_2SO_4$ bath with the additives (PEG and Cl^-) at room temperature [13]. Only when both PEG and Cl^- additives are added in the bath does the growth mechanism lead to Cu nanotubes rather than solid metallic nanowires, Figs. 2(a) and (b). The electrodeposited Cu nanotubes are converted to Cu_2O by oxygen plasma treatment. This plasma ash technique is commonly used to remove organic residues after the processing in the semiconductor or packaging industries. The oxygen plasma technique was found to be efficient in the conversion of the deposited Cu in nanotube format to Cu_2O oxides. The microstructure of the Cu_2O nanotube arrays studied by SEM is shown in Figs. 3 (a) and (b).

XRD analysis of the Cu nanotubes prior to conversion to the oxide shows polycrystalline phases of 100, 200 and 220 orientation in Fig. 4(a). The oxidised nanotubes XRD data

(Fig. 4(b)) shows typical Cu_2O phases of 111, 200, 211, 220, 311 and 222 in addition to the non-oxidised Cu metal phases. The polycrystalline nanotubes containing both Cu_2O and Cu phases clearly indicates that the metallic Cu tubes have not been completely converted to oxides during the 4.5 minutes plasma treatment at 250 W. The oxidation time at a fixed power (250 W) was varied to achieve a minimum metallic tube wall thickness as the inner core support of the outer shell oxide layers. The conversion rates of Cu thin film and Cu nanotubes to Cu_2O are shown in Fig. 5. The electrodeposited Cu thin film and Cu nanotubes of 3 cm^2 area and 20 μm long nanotubes were oxidised for the times shown. The formed oxide layers were chemically removed in a commercial oxide removal solution (Schloetter S20 - sulphuric acid based). The weight loss due to the oxide layer removal in this solution (Mettler Toledo XS105, repeatability (SD) = 0.02 mg) is plotted against the oxidation time in Fig. 5(a), which gives the conversion rate plot. The Cu_2O conversation rate is correlated with the wall thickness of Cu metallic tubes as shown in Fig. 5(b) e.g., for 4.1 mins plasma treatment at the specified power of 250 W it is estimated to be 30 nm based on the weight loss on removing the oxide and assuming the Cu_2O density of 6.09 g/cm^3. The thickness of the Cu_2O is assumed to be 15 nm on both inner and outer nanotube walls and the remaining un-oxidised Cu nanotube support is approximately 45 nm, (given an outer tube diameter of 300 nm and inner diameter 150 nm. SEM images of the Cu nanotubes as deposited, after oxygen plasma treatment and after oxide removal are shown in figures 6 (a to c) respectively. The thinned Cu core substrate after the process of oxide formation and removal is seen by comparing Figs 6(a) and 6(c).

The electrochemical performance of the Cu_2O nanotubes was studied by cyclic voltammetry. Fig. 7(a) shows the first 20 cycles for Cu_2O nanotubes with low oxide

content (~ 8 nm, or 2.32 mg / 3 cm^2, from oxygen plasma treatment for 1 min) at a sweep rate of 0.5 mV/s. In the first cycle, there is one broad cathodic peak located at 1.10 V and a small shoulder at 0.7 V, while in the following cycles three distinct cathodic reactions are observed at 1.55, 0.7 and approaching 0 V respectively. The peak at 1.10 V can be assigned to the Li^+ insertion reaction into Cu_2O and irreversible electrolyte reaction products that are not present in the second or subsequent cycles. The three regions in the following cycles are attributed to the Li^+ insertion reaction into Cu_2O crystallites [14-15]. The potential of the Li^+ insertion reactions and the formation of the protective interphase layer in the first cycle are so close that they appear as a broad single peak. Meanwhile, one extended oxidation wave starting at 0.2 V up to a peak at 2.55 V corresponds to Li^+ de-insertion from the crystal lattice of Cu_2O nanotubes. It also can be seen from Fig. 7(a) that the potential of the Li^+ insertion reaction increases in the cycles following the first.

Cu_2O is among a group of metal oxides that demonstrate a novel reactivity mechanism which differs from the classical Li^+ insertion or de-insertion and involves the formation and decomposition of Li_2O [5]. Cu_2O transfers two electrons in the electrochemical reaction (with a theoretical capacity of 375 $mAhg^{-1}$) and such reduction enables the conversion into nanocomposite materials consisting of nanometre scale Cu metallic clusters in the range 1 to 5 nanometres as reported by Tarascon et al. dispersed in an amorphous Li_2O matrix, according to the following redox reaction [5].

$$Cu_2O + 2Li^+ + 2e^- \rightarrow 2Cu + Li_2O \qquad [1]$$

The SEM image (Fig. 3a) shows that oxide morphology is not uniform along the nanotubes. At the beginning of the reaction, the particle size of Cu_2O on the nanotubes is

inhomogeneous. The SEM images of Fig. 11 (a) and (b) indicate the formation of homogeneous nanosized Cu_2O crystallites during the conversion reaction in Li cycling. The formation of homogeneous Cu_2O crystallite morphology leads to uniform reactivity towards Li and the consequent dispersion of nanometre scale Cu metallic clusters in the amorphous Li_2O improves the reversibility of Li_2O back to Li in the charge cycle due to interconnected network between the Li_2O particles. Therefore, the potential of the Li^+ insertion reaction into Cu_2O increases after the first cycle and remains constant in all the following cycles showing balanced discharge-charge behaviour. The complete overlapping of the cyclic voltammograms in continueous cycling indicates the reversibilty of Li^+ insertion and de-insertion reactions in Cu_2O due to the homogeneous crystallites on the nanotube supports. Fig. 7(b) is a discharge-charge curve of Li^+ in Cu_2O nanotubes by cyclic voltammetry showing the specifice Li storage capacity is still around 375 $mAhg^{-1}$ after 30 cycles with no significant deterioration. Additionally, the increased surface area of Cu_2O nanotubes due to the inner wall and the open tube end provides electrolyte access and support for fast ionic mass transport to the remote electrode area. The capacity retention of the self-supported Cu_2O nanotube electrodes may be attributed to the short Li^+ and e^- transport length, easy penetration of electrolyte into the pores and increased electrolytic contact area. The irreversible capacity loss in the first cycle is caused by irreversible electrolyte reactions at the Cu_2O lattice surface, which hinders lithium ion movement to the anode [16-17]. These irreversible reactions are significant in nano-architectured electrodes because of the large surface and interface areas [18] but their formation decreases with cycling [19]. The irreversible capacity loss in the first cycle is also partly associated with the irreversible conversion reaction of Li_2O due to lack of interconnected network formed between Li_2O particles by nanosized Cu metallic

clusters. In this work the loss is apparent only on the first cycle and there are no additional irreversible peaks in the cathodic sweep.

In another experiment thicker Cu_2O nanotubes were formed by oxygen plasma treatment for 4.5 min and according to the conversion correlation curve (Fig. 5(b)), about 34 nm of the solid Cu is converted to equilvalent Cu_2O. Fig. 8(a) shows the first three voltammograms of the Cu_2O nanotubes recorded at a sweep rate of 0.5 mV/s. These curves show the same characteristics but higher current density (1.5 mA/cm^2) as seen for low content Cu_2O electrodes at the same sweep rate. When the sweep rate is increased to 2 mV/s or 5 mV/s the current density increases but the shape of cyclic voltammograms is altered both in the cathodic or anodic regions, Fig. 8(b). At the higher sweep rate the cathodic peaks at 0.7 V and 1.15 V are a single wave until sweep reversal at 0 V while in the anodic region an oxidation peak is generated in the range of 0.5-1.0 V in addition to the peak at 2.55 V. The capacities in the potential range are the same as those recorded at slower sweep rates. Additionally, the polycrystalline Cu_2O particles converted to homogeneous nanoparticulates with cycling may possess additional crystalline imperfections and grain boundary sites for hosting Li^+ ions. The charge-discharge capacity curves for low and high sweep rates are shown in Fig. 8(c).

At the slower sweep rate (0.5 mV/s), the discharge and charge capacities started with higher values and decreased due to the particle size effect. As mentioned in the previous section, the conversion reactions during Li^+ insertion/de-insertion produce homogeneous nanoparticles of Cu_2O, Cu and Li_2O however, due to the higher quantity of Cu_2O a large numbers of cycles (first 20 cycles) are required to achieve uniform particles size. Once the particles size are consistent, the discharge-charge capacity increases and stabilises

from 31st cycle forwards with slightly higher capacity (401 $mAhg^{-1}$) than that recorded for the earlier sample with thin oxide outside the Cu support. The higher specific capacity may be attributed to the presence of a large amount of Cu nanodomains during the charging process which form an interconnected network between Li_2O particles and could thereby enhance the reactivity of Li_2O reconversion to Cu_2O due to the high surface activity as well as electronic conductivity in the recharging process [5, 14].

When the same Cu_2O nanotubes are cycled at 5 and 2 mV/s each for 20 consecutive cycles (Fig. 7(b)) the initial capacity (388 $mAhg^{-1}$) for both cases is consistent with the above observation for the slower sweep rate (Fig. 8(c)). The slight decrease in Li^+ storage capacity of Cu_2O nanotubes may be indicative of the lower Li^+ insertion/de-insertion rates in the same potential intervals at higher sweep rates. The rate capability performance of Cu_2O nanotubes measured after 80 cyclic voltammograms as described above and cycles at three current densities of 1.67 mA/cm^2, 3.33 mA/cm^2 and 5 mA/cm^2 are shown in Fig. 9(a - c). There are three clear potential ranges at 3.0 - 1.75 V, 1.25 – 0.35 V and 0.35 – 0 V in the curves as shown in Fig. 9(a) and (b) consistent with three cathodic peaks in the cyclic voltammograms. The discharge-charge plateau appears as a smooth shoulder at the current density of 5 mA/cm^2 (Fig. 9(c)). The specific capacities at 1.677 mA/cm^2 (455 $mAhg^{-1}$), 3.33 mA/cm^2 (450 $mAhg^{-1}$) and 5 mA/cm^2 (440 $mAhg^{-1}$) are quite similar for each of the current densities investigated. Therefore it is clear that the rate capability perforamance of Cu_2O nanotubes can be as high as 5 mA/cm^2 with little decrease in the available capacity of the core/shell electrode material.

Subsequently, the same Cu_2O electrode was cycled at constant current density of 1.67 mA/cm^2 and a time limited total charge-discharge of 1 hour. Fig. 10 shows the last 11

discharge-charge curves started from 84th cycle. It can be seen from the graph that initially the discharge-charge curve reaches a potential minimum of 0 V but in later cycles reversed at approximately 0.65 V vs. Li/Li^{+}. Initially the limited time was sufficient to utlise the full Li storage capacity (455 mAhg^{-1}) of the Cu_2O nanotubes. However, utilisation of additional capacity generated over cycling by the Cu_2O electrode required a longer cycle time. Therefore, the lower potential limit achieved during discharge shifts to the more positive potential with cycling. The cycling performances of Cu_2O nanotubes shows a high level of structural integrity as capacity was retained even after 94 cycles when cycled at 1.67 mA/cm^2. The structural integrity and consequnt long cycleability is also supported by SEM images taken after Li cycling, see Fig. 11(a and b). The Cu_2O nanotubes remained free standing on the substrate with uniform nanosized particles formed with cycling. The observed SEM images are consistent with the explanations given earlier for the higher capacity of Cu_2O nanotubes in terms of homogeneous nanoparticles size effects during the conversion reactions.

To explain the enhanced cyclability of the structures reported in this work two types of Cu_2O nanotubes must be considered. We studied Cu_2O nanotubes (i) with no metallic Cu, and (ii) with metallic Cu as inner support. When Cu nanotubes are fully converted to Cu_2O very low cycleability is observed. After 20 cycles (at 0.5 mV/s vs Li) the retention capacity is reduced to 10% of the initial value, see Fig. 12.

To explain the electron-conducting mechanism and structural integrity of Cu_2O nanotubes we propose the following, see Fig. 13. In the case of the Cu_2O nanotubes with metallic Cu as the inner core support with high electrical conductivity, Fig. 13(a), the reaction commences along the full length of the nanotube walls and structural and

electrical integrity is maintained in this core(metal)/shell(oxide) type structure upon Li^+ insertion, Fig 13(b), and extraction Fig 13(c).

For fully converetd Cu_2O nanotubes Fig 13(d), the conversion reaction starts at the base connection with the substrate and then gradually propagates through the nanotubes. Fig 13 (e) is representative of a point close to the base of the nanotube where all of the Cu_2O converts to Cu and Li_2O. Further up the nanotube not all of the tube will convert as the electrical conductivity of the Cu_2O will not support a relatively high reaction and conversion rate. On the subsequent Li^+ extraction less Li will be removed as the nanoscale particles of Cu will not have sufficient interconnectivity to facilitate the conversion reaction, Fig 13(f). Again this reaction will be exacerbated further up the 20 μm long nanotubes. This leads to the poor cycliability recorded in Fig. 12 for the substrate where all of the Cu core was oxidised to Cu_2O prior to lithium test.

Conclusion

A direct electrodeposition technique for high quality Cu nanotube arrays and subsequent conversion of the deposited Cu into Cu_2O has been developed. The Cu_2O nanotube arrays have shown high capacity, cycleability and rate capability. The cycling performance of Cu_2O nanotubes shows a high level of structural integrity with capacity retention even after 94 cycles when cycled at 1.67 mA/cm^2 (approximately 1C rate). The electrochemical performance of the Cu_2O nanotubes is enhanced by the high surface area, easy infiltration of electrolytes, high electrical conductivity of Cu support and structural integrity. The Cu_2O nanotubes also eliminate the requirment of ancillary materials typically used in Li-ion batteries, such as carbon particles to increase conductivity.

Acknowledgments

Enterprise Ireland Technology Development Project CFTD/05/IT/317.

References

1. C. R. Sides and C. R. Martin, *Nanomaterials in Li-ion battery electrode design*, *Modern aspects of Electrochemistry*, No. 40, R. E. White Editor, 75, Springer, New York (2007).
2. N. Li, C.R. Martin and B. Scrosati, *J. Power Sources*. **97**, 933 (2001).
3. Y. Wang and G. Cao, *Adv. Mater.*, **20**, 2251 (2008).
4. J. H. Kim, S. Khanal, M. Islam, A. Khatri and D. Choi, *Electrochem. Commun.*, **10**, 1668 (2008).
5. P. Poizot, S. Laruelle, S. Grugeon, L. Dupont and J.-M. Tarascon, *Nature*, **407**, 496 (2000).
6. P.L. Taberna, S. Mitra, P. Poizot, P. Simon and J.-M. Tarascon, *Nat. Mater.*, **5**, 567 (2006).
7. Y. Li, B. Tan and Y. Wu, *Nano Lett.*, **8**, 265 (2008).
8. S. Grugeon, S. Laruelle, R.H Urbina, L. Dupont, P. Poizot and J.-M. Tarascon, *J. Electrochem. Soc.*, **148**, A285 (2001).
9. R. Inguanta, S. Piazza and C. Sunseri, *Electrochim. Acta*, **53**, 6504 (2008).
10. S. Wang, Q. Huang, X. Wen, X-Y. Li and S. Yang, *Phys. Chem. Chem. Phys.*, **4**, 3425 (2002).
11. A. M. Hermann, P. A. Ramkrishnan, V. Badri, P. Mardilovich and W. Landuyt, *Int. J. Hydrogen Energy*, **26**, 1295 (2001).
12. C. Mu, Y. Yu, R. Wang, K. Wu, D. Xu and G. Guo, *Adv. Mater.*, **16**, 1550 (2004).
13. T. Chowdhury, D.P. Casey and J.F. Rohan, *Electrochem. Commun.*, **11**, 1203 (2009).

14. Y.H. Lee, I.C. Leu, S.T. Chang, C.L. Liao and K.Z. Fung. *Electrochim. Acta*, **50**, 553 (2004).
15. C.Q. Zhang, J.P. Tu, X.H. Huang, Y.F. Yuan, X.T. Chen and F. Mao, *J. Alloy Compd.*, **441**, 52 (2007).
16. L.Y. Beaulieu, S.D. Beattie, T.D. Hatchard and J.R. Dahn, *J. Electrochem. Soc.*, **150,** A419 (2003).
17. N. Pereira, L.C. Klein and G.G. Amatucci, *Solid Sate Ionics*, **167**, 29 (2004).
18. H.-C. Shin and M. Liu, *Adv. Funct. Mater*, **15**, 582 (2005).
19. M. Inaba, T. Uno and A. Tasaka, *J. Power Sources*, **146,** 473 (2005).

Figures.

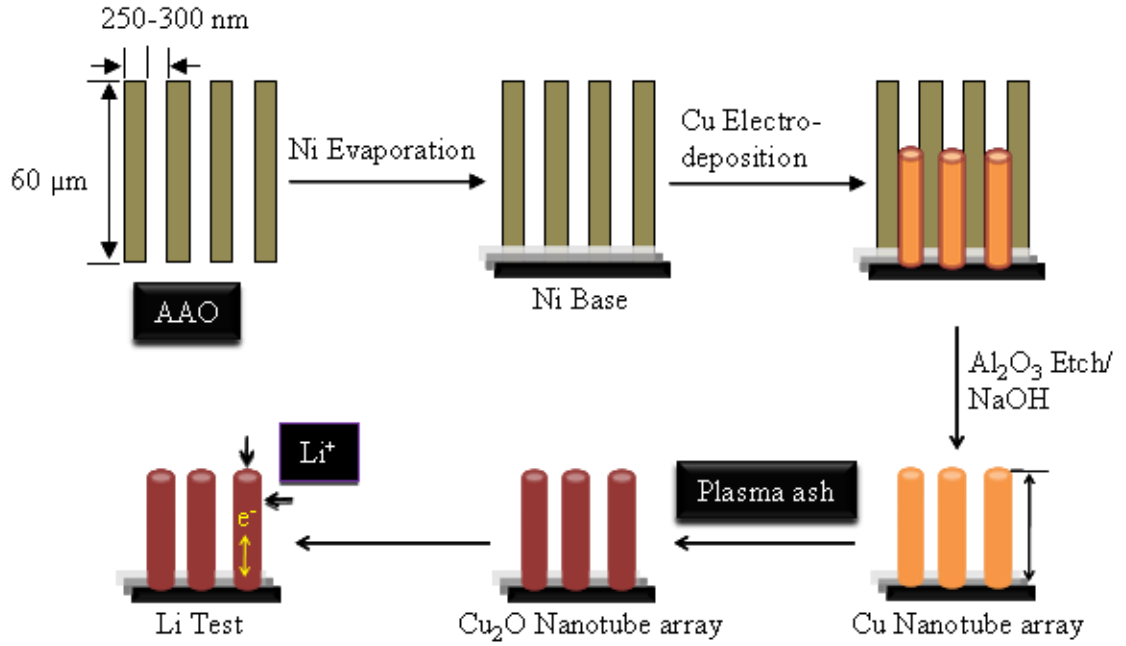

Figure 1. Schematic illustration of the synthesis process for high aspect ratio Cu_2O nanotube arrays.

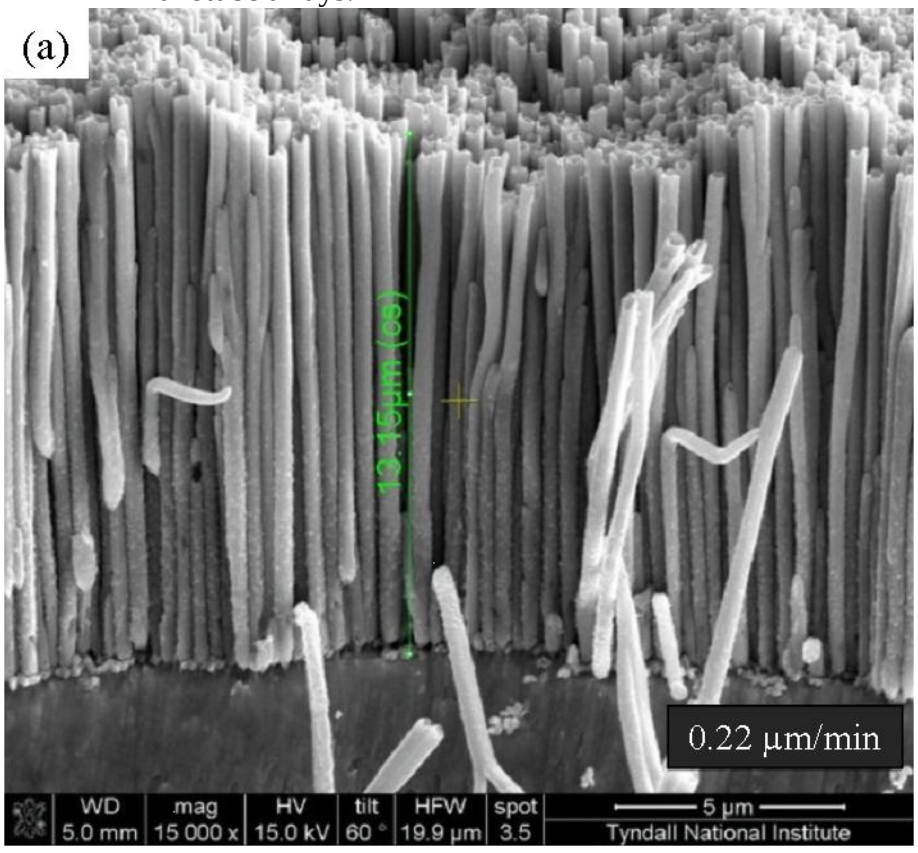

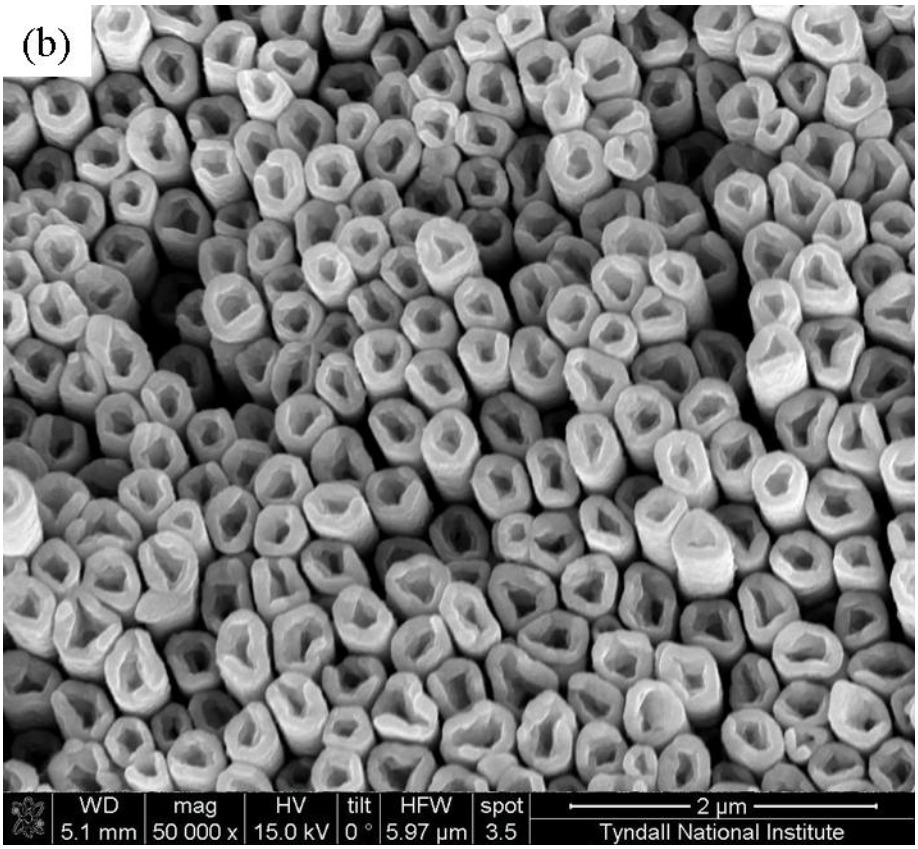

Figure 2. SEM images of as-synthesised Cu nanotube arrays, (a) cross-sectional and (b) plan view.

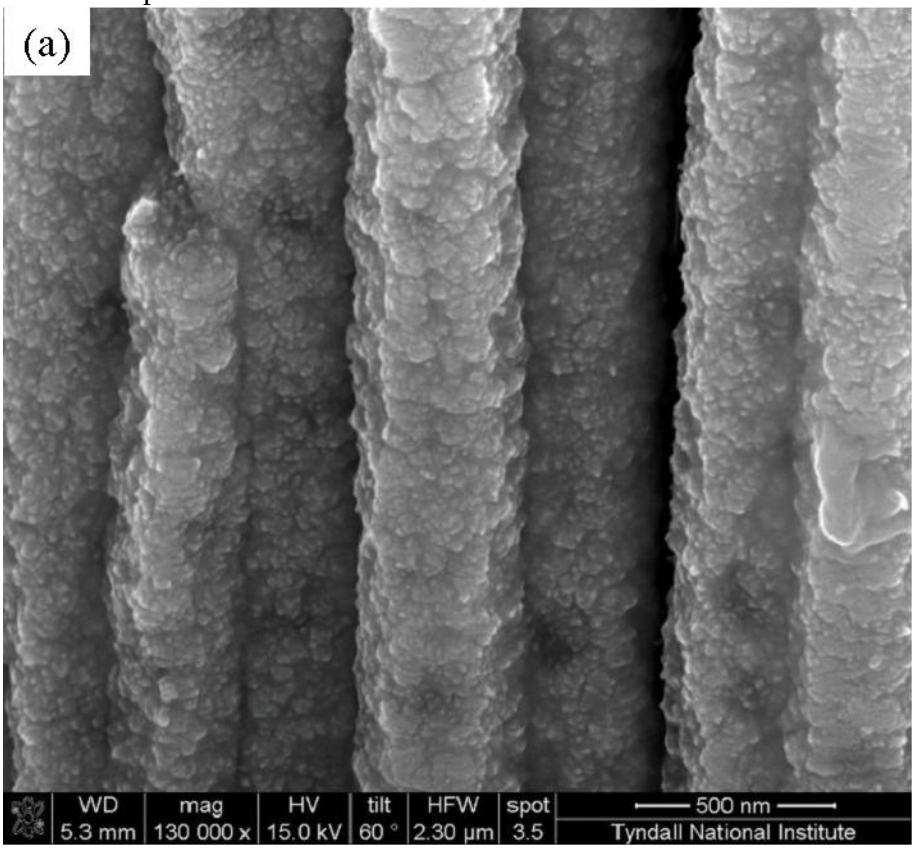

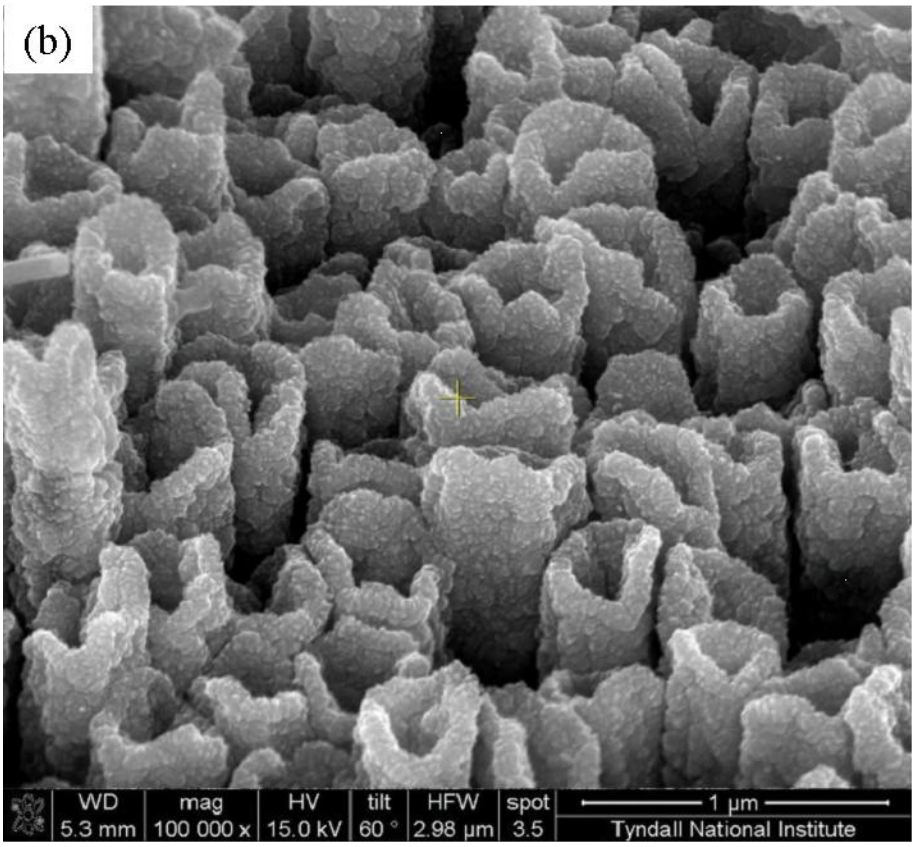

Figure 3. SEM images of the Cu_2O nanotube arrays obtained from Cu nanotubes after oxygen plasma treatment for 4.5 minutes, (a) cross-sectional and b) plan view.

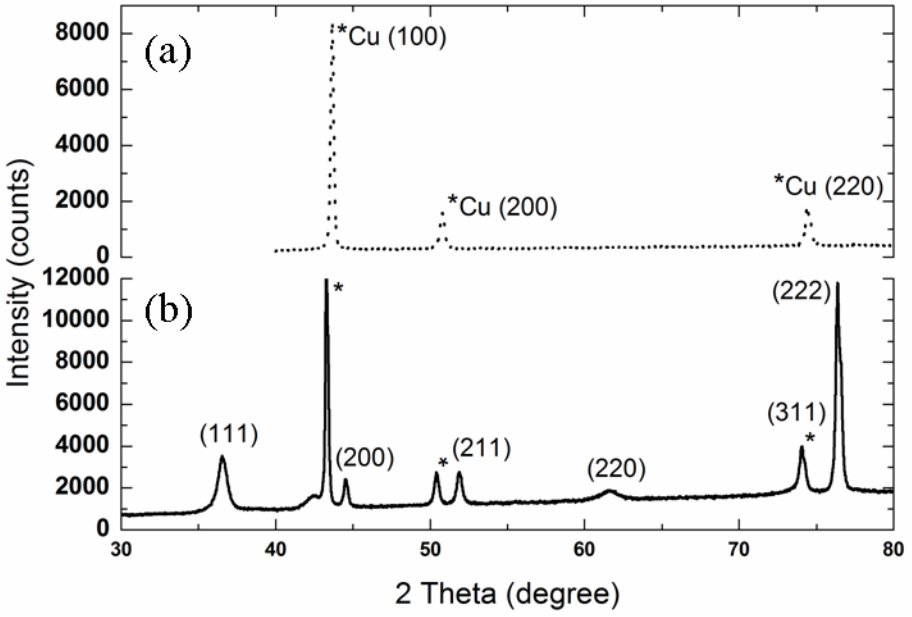

Figure 4. XRD patterns of (a) Cu nanotubes after removal of the AAO template and (b) Cu_2O nanotubes (oxygen plasma treatment 4.5 minutes).

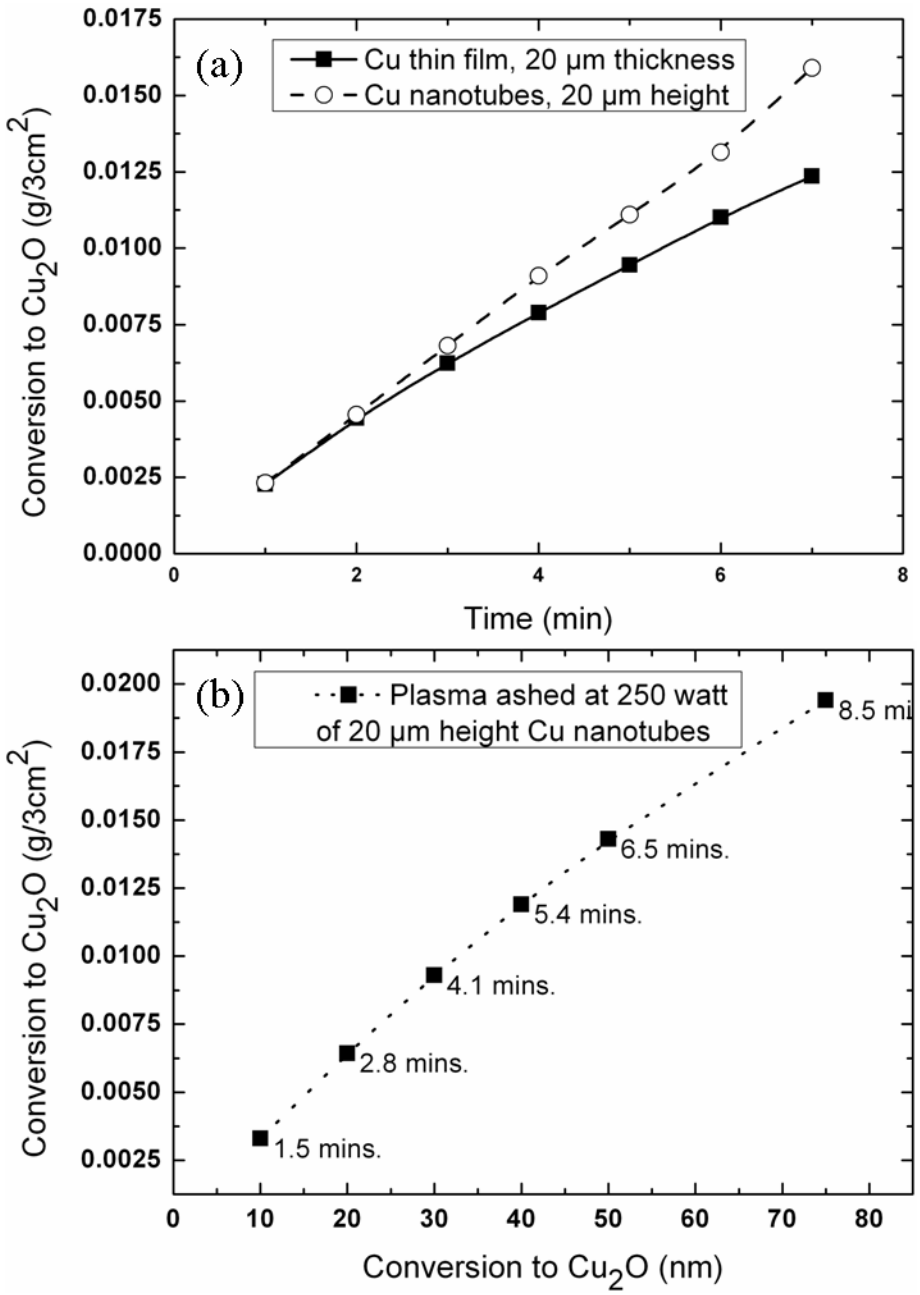

Figure 5. Conversion rate plots for Cu to Cu_2O by oxygen plasma treatment, (a) time related plot and (b) correlation plot for a series of oxygen plasma times.

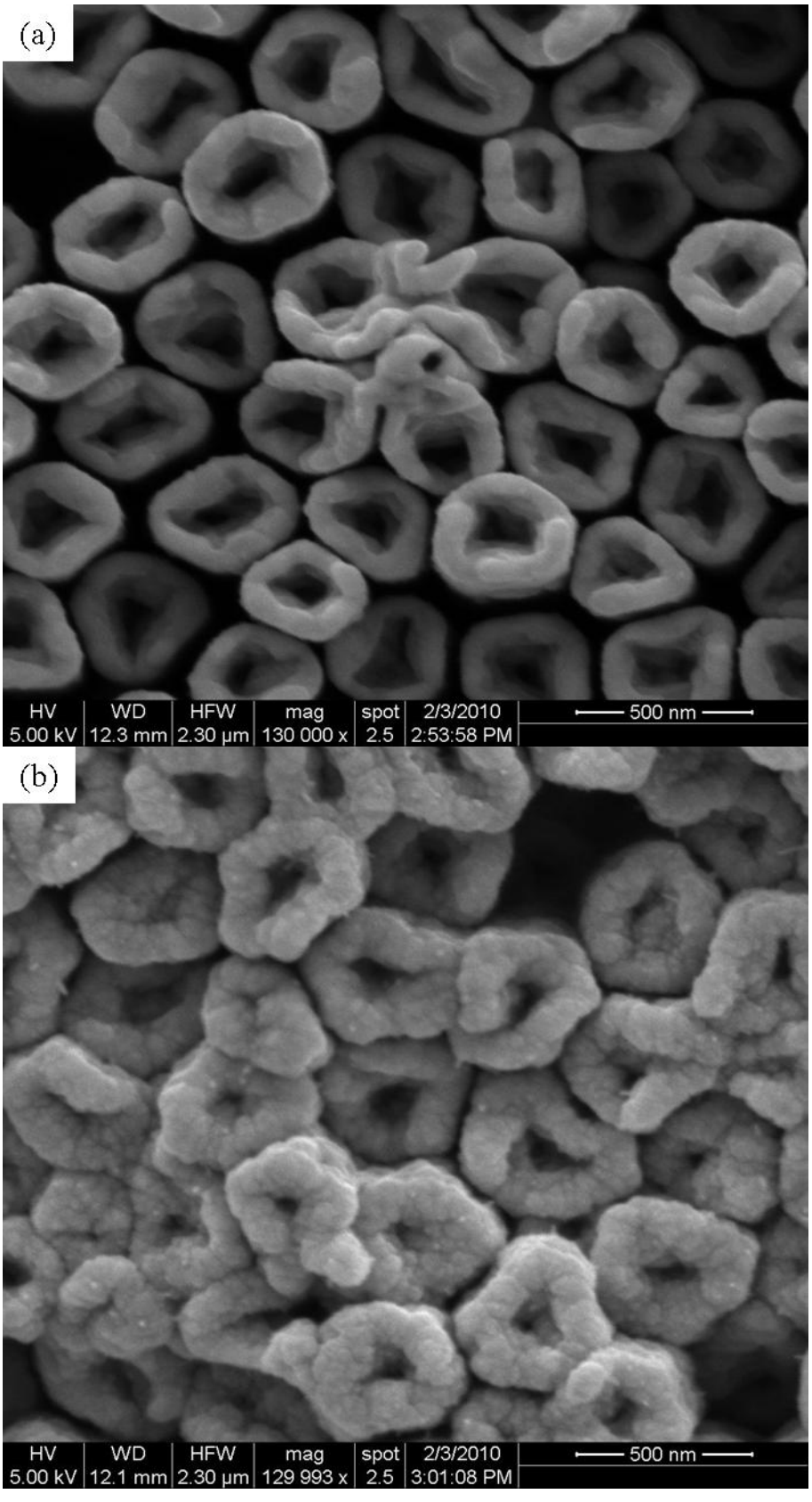
(a)
HV
5.00 kV
WD
12.3 mm
HFW
2.30 µm
mag
130 000 x
spot
2.5
2/3/2010
2:53:58 PM
500 nm
(b)
HV
5.00 kV
WD
12.1 mm
HFW
2.30 µm
mag
129 993 x
spot
2.5
2/3/2010
3:01:08 PM
500 nm

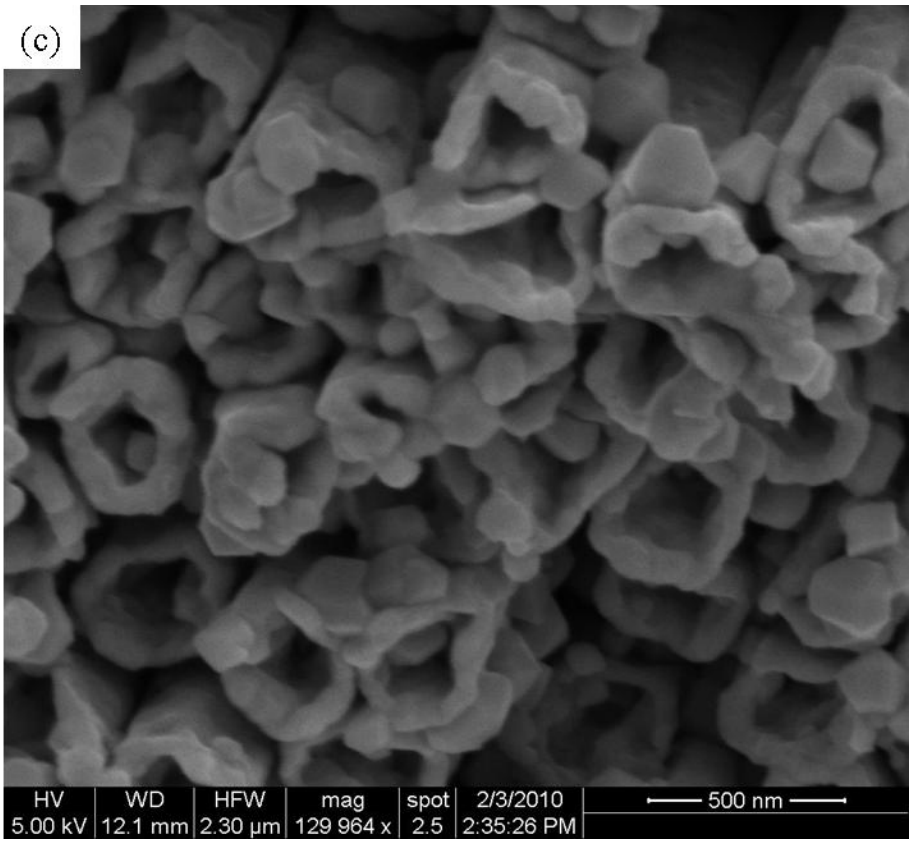

Figure.6 SEM image of (a) Cu nanotubes, (b) Cu_2O nanotubes (oxygen plasma treatment for 4.1 mins) and (c) Thinned Cu metal core support after oxide removal by Schloetter S20 (sulphuric acid based) solution.

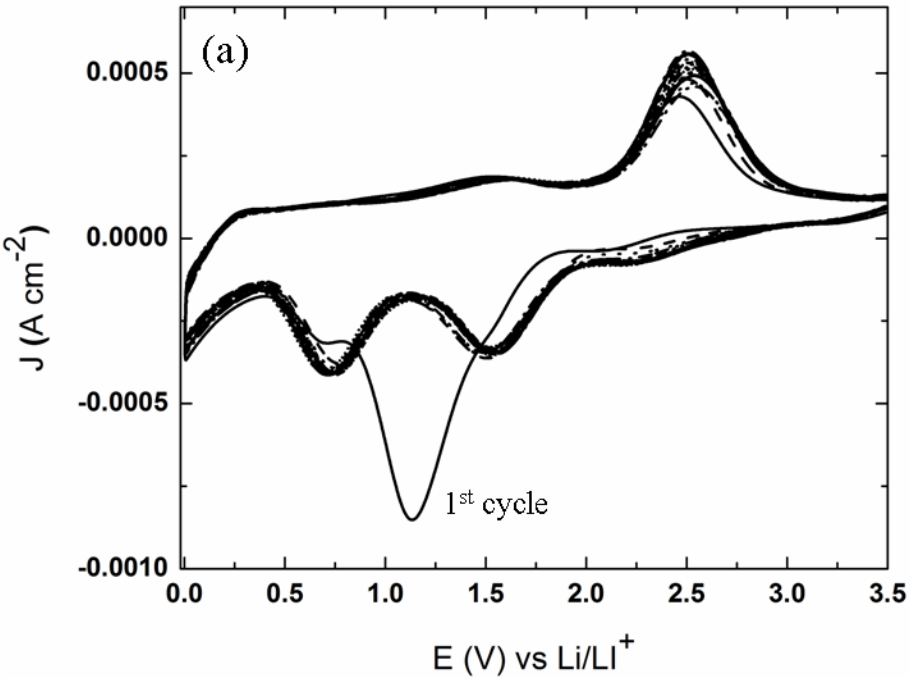

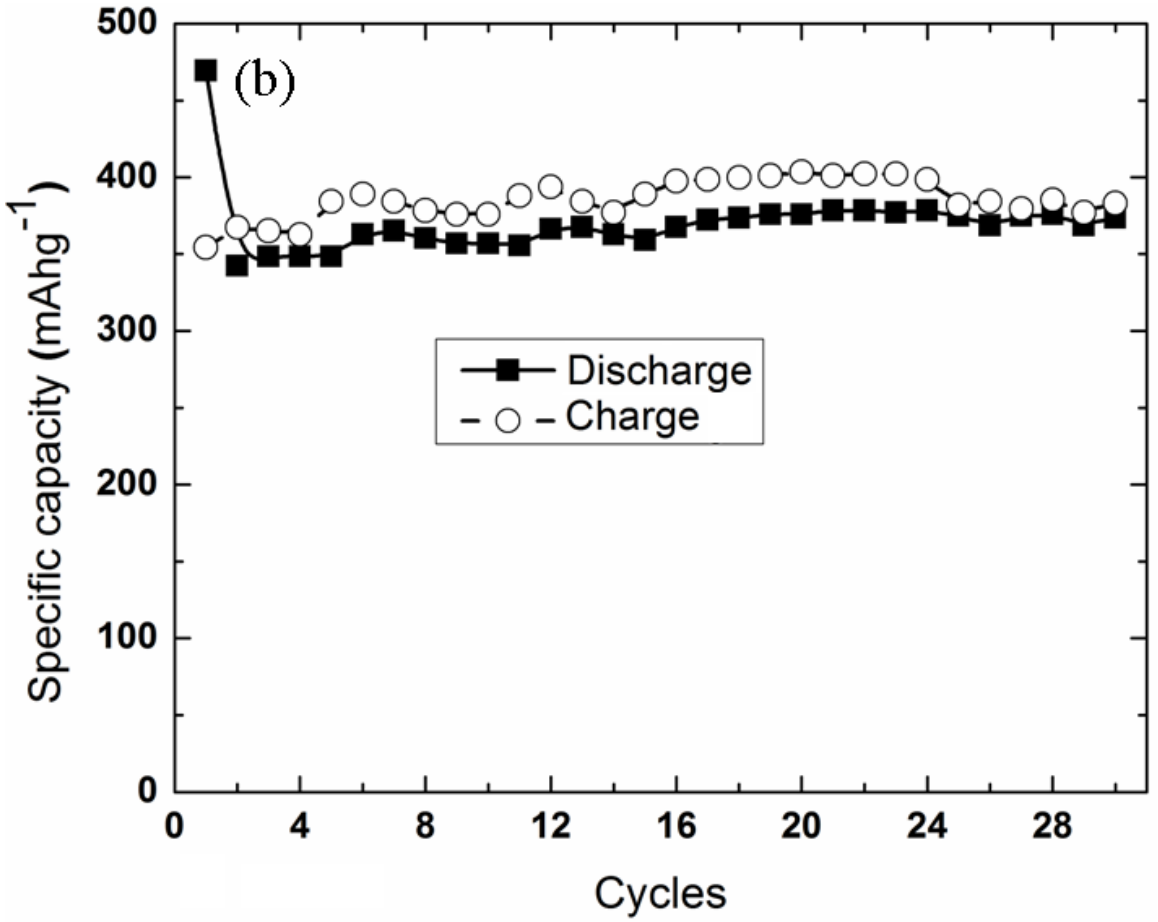

Figure 7. (a) First 20 cyclic voltammograms of Cu_2O nanotubes (oxygen plasma treatment for 1 min) Sweep rate 0.5 mV/s, and (b) Discharge-charge capacity vs. cycle number for 30 cycles of the Cu_2O nanotubes.

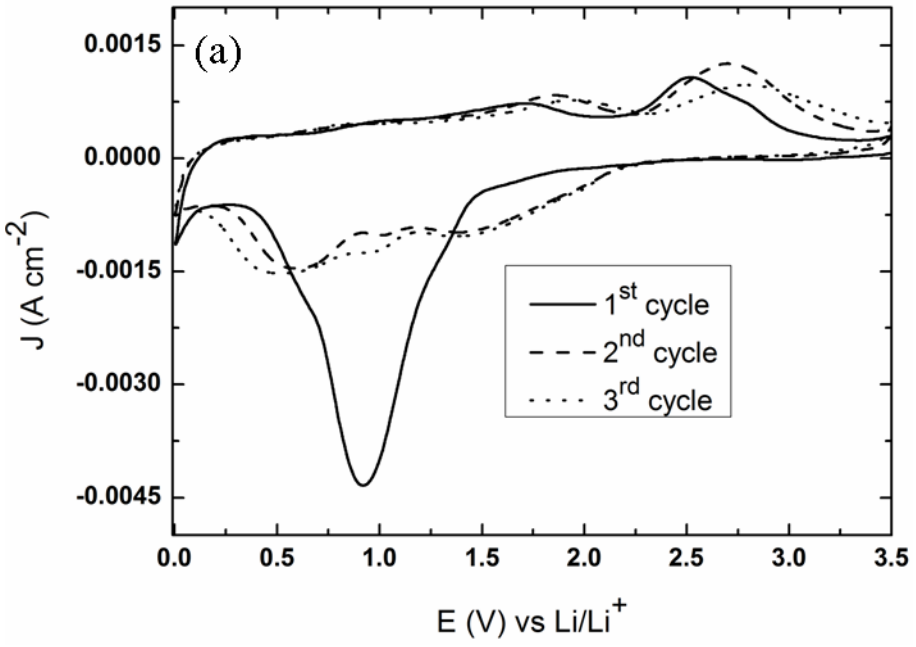

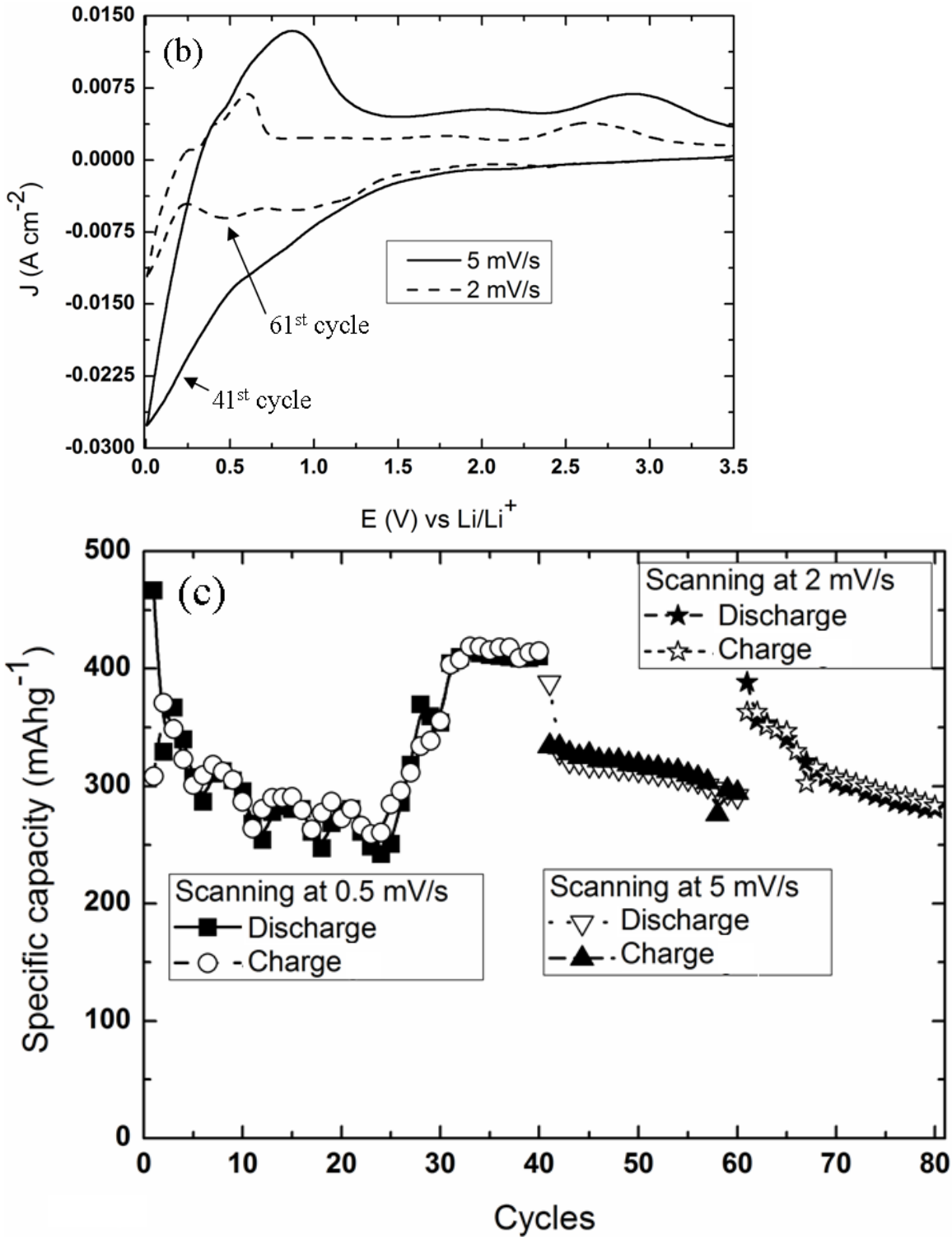

Figure 8. (a) First 3 cyclic voltammograms of Cu_2O nanotubes (oxygen plasma treatment for 4.5 min). Sweep rate 0.5 mV/s, (b) 41st and 61st cyclic voltammograms of Cu_2O nanotubes with sweep rate of 5 mV/s and 2 mV/s, respectively, (c) Discharge-charge capacity vs. cycle number curves of Cu_2O nanotubes for 80 cycles at various sweep rates.

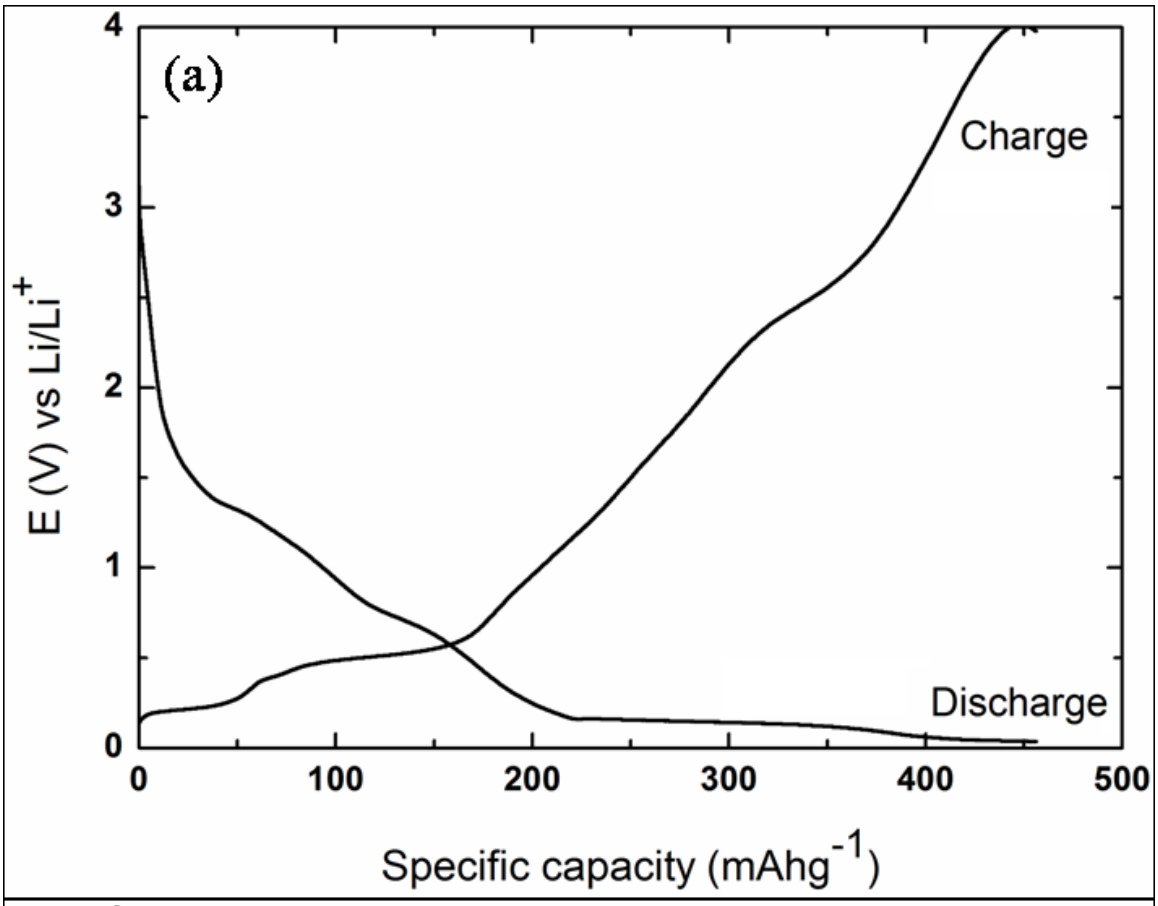
(a)
Charge
Discharge
E (V) vs Li/Li+
Specific capacity (mAhg-1)
0
1
2
3
4
0
100
200
300
400
500

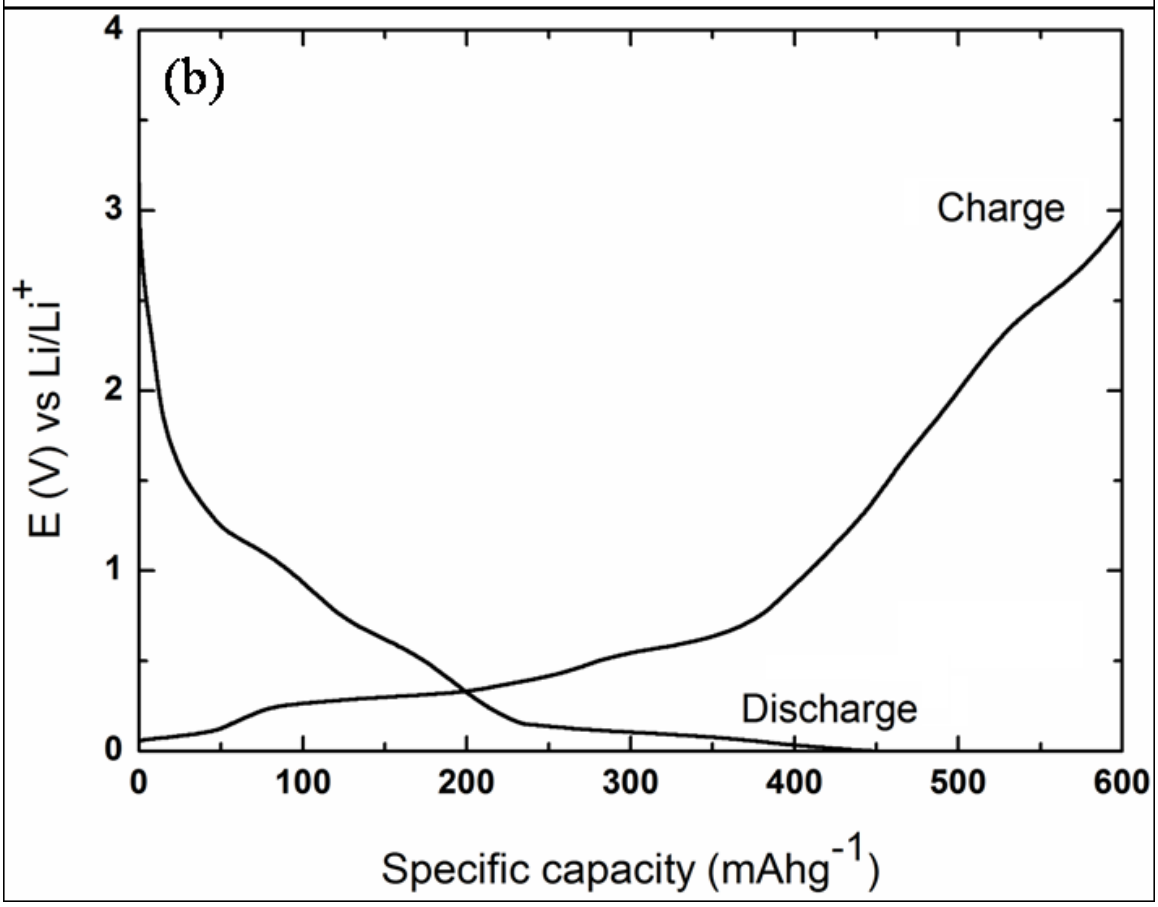
(b)
Charge
Discharge
E (V) vs Li/Li+
Specific capacity (mAhg-1)
0
1
2
3
4
0
100
200
300
400
500
600

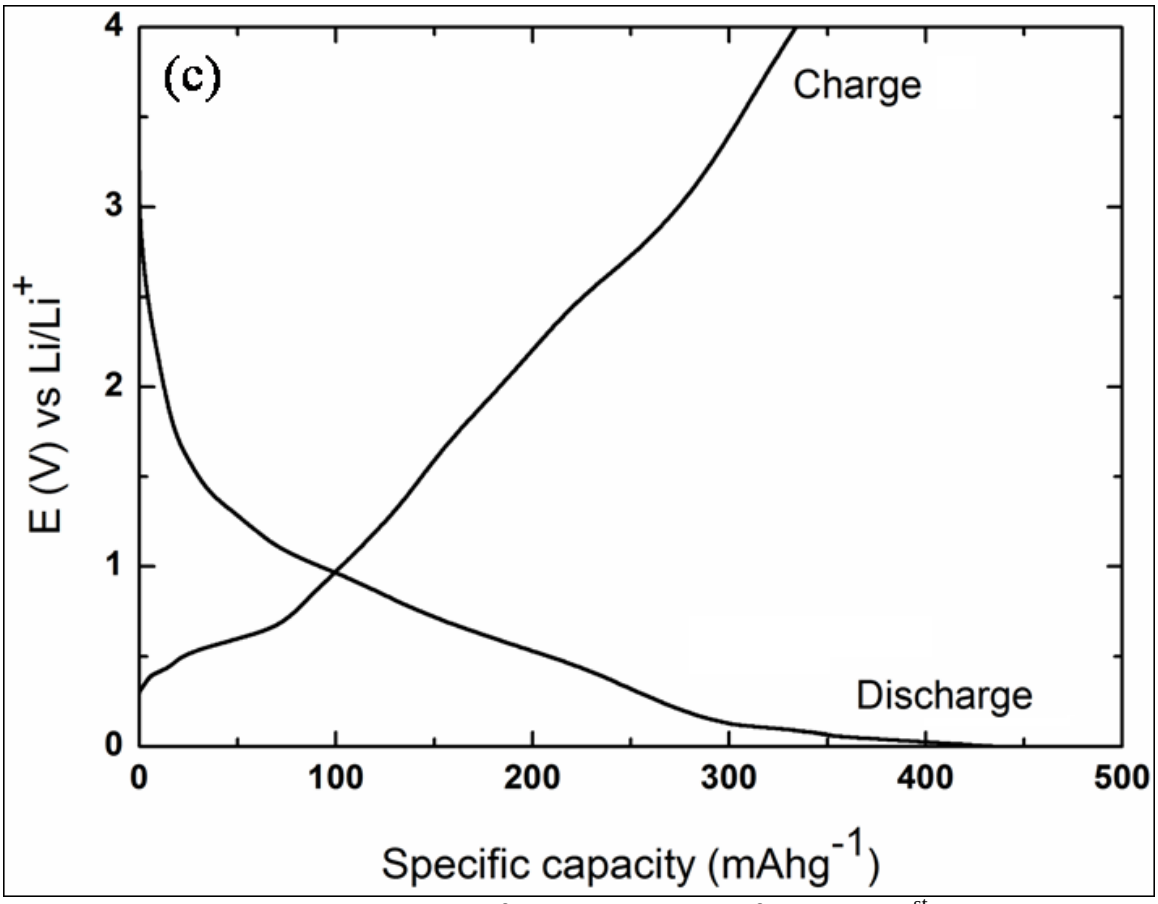

Figure 9. Discharge-charge curves of Cu_2O nanotubes from the 81st cycle at current densities of (a) 1.67 mA/cm^2, (b) 3.33 mA/cm^2 and (c) 5 mA/cm^2.

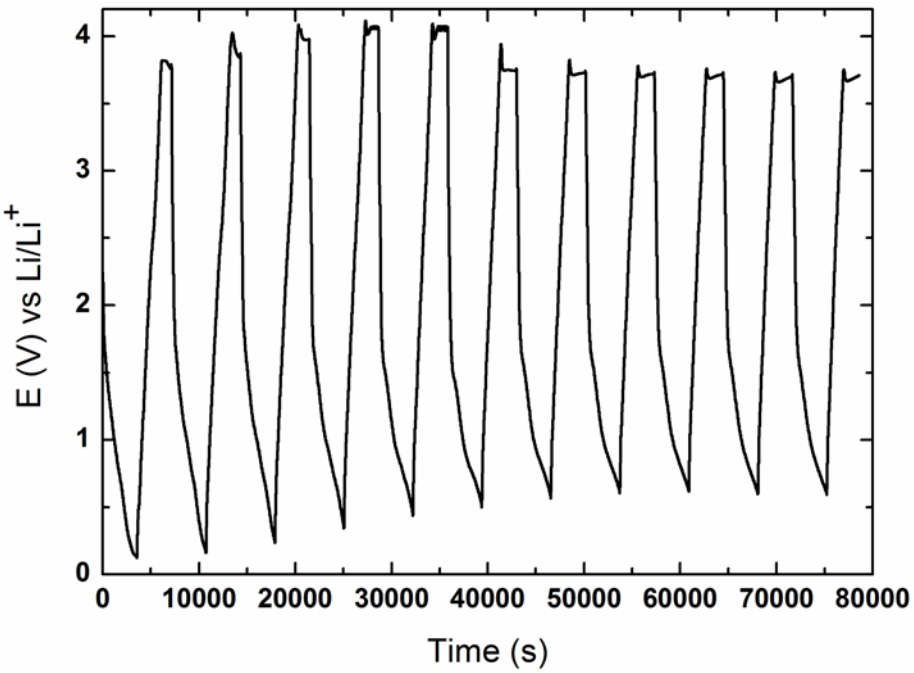

Figure 10. Discharge-charge curves of Cu_2O nanotubes from 84th cycle at current density of 1.67 mA/cm^2 for 11 cycles.

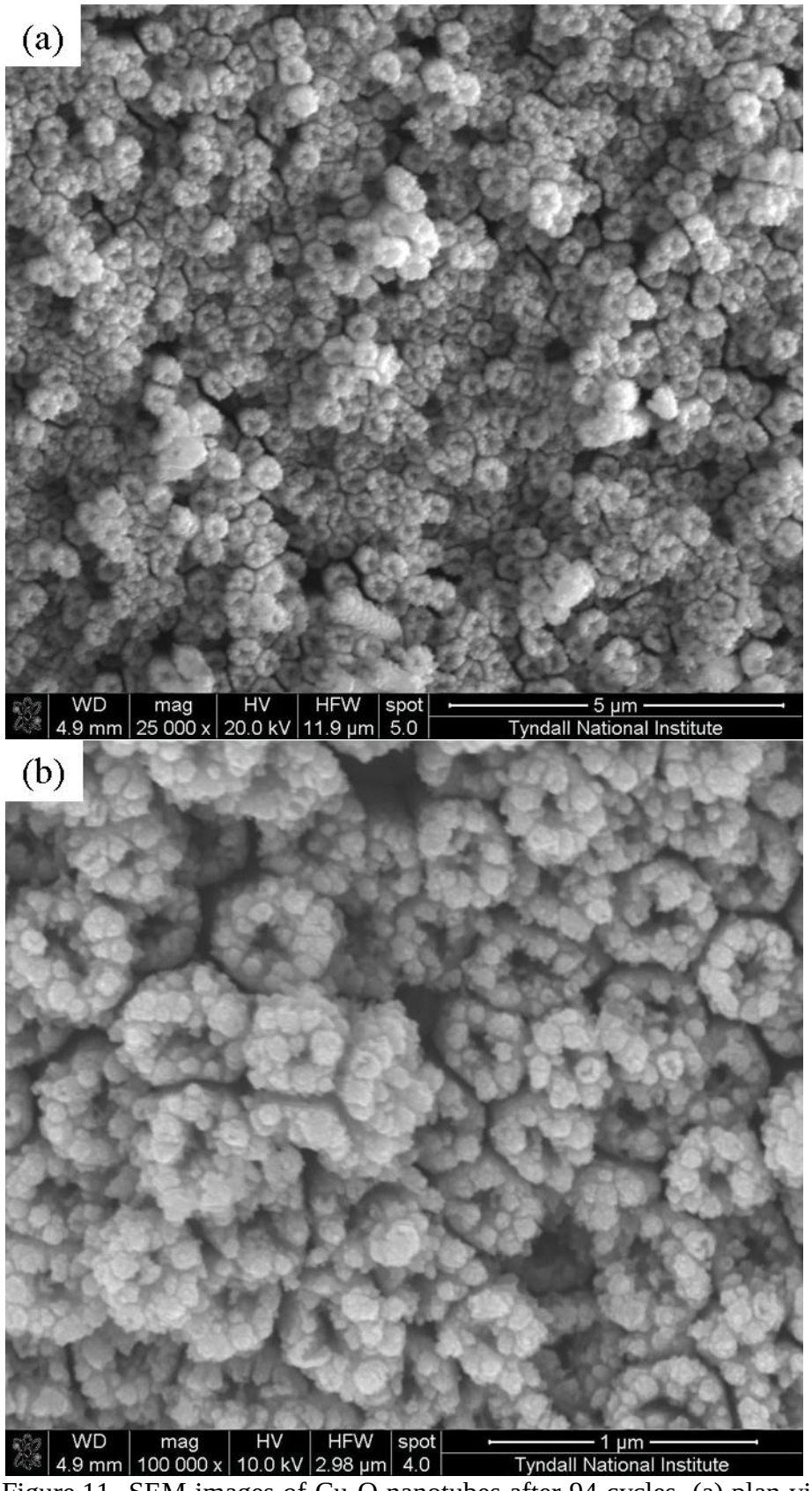

Figure 11. SEM images of Cu_2O nanotubes after 94 cycles, (a) plan view, magnification x25,000 and (b) plan view, high magnification x100,000.

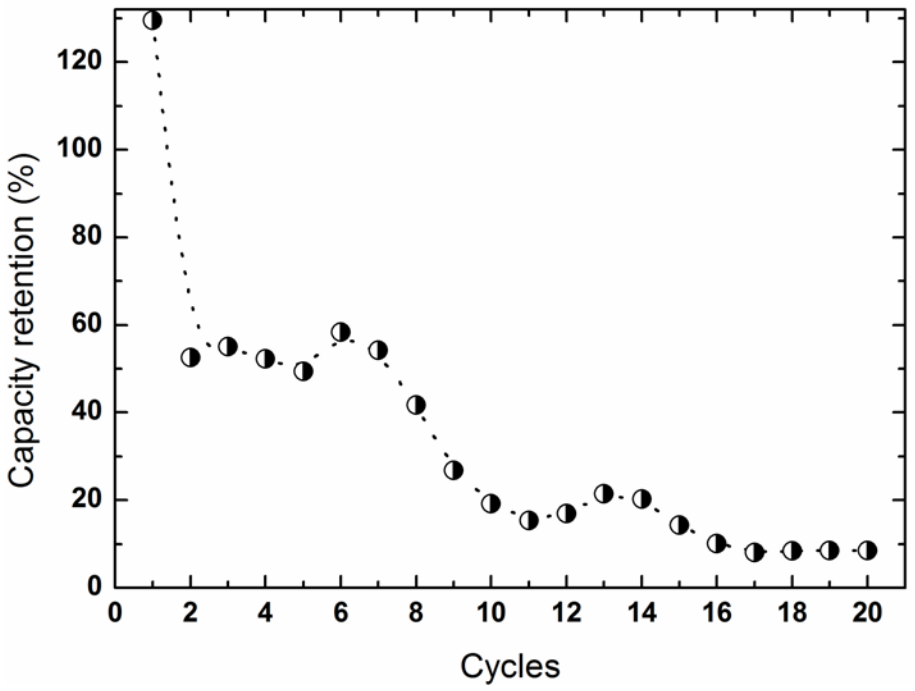

Figure 12. Capacity retention vs cycle number curve of Cu_2O nanotubes (fully converted) with sweep rate of 0.5 mV/s.

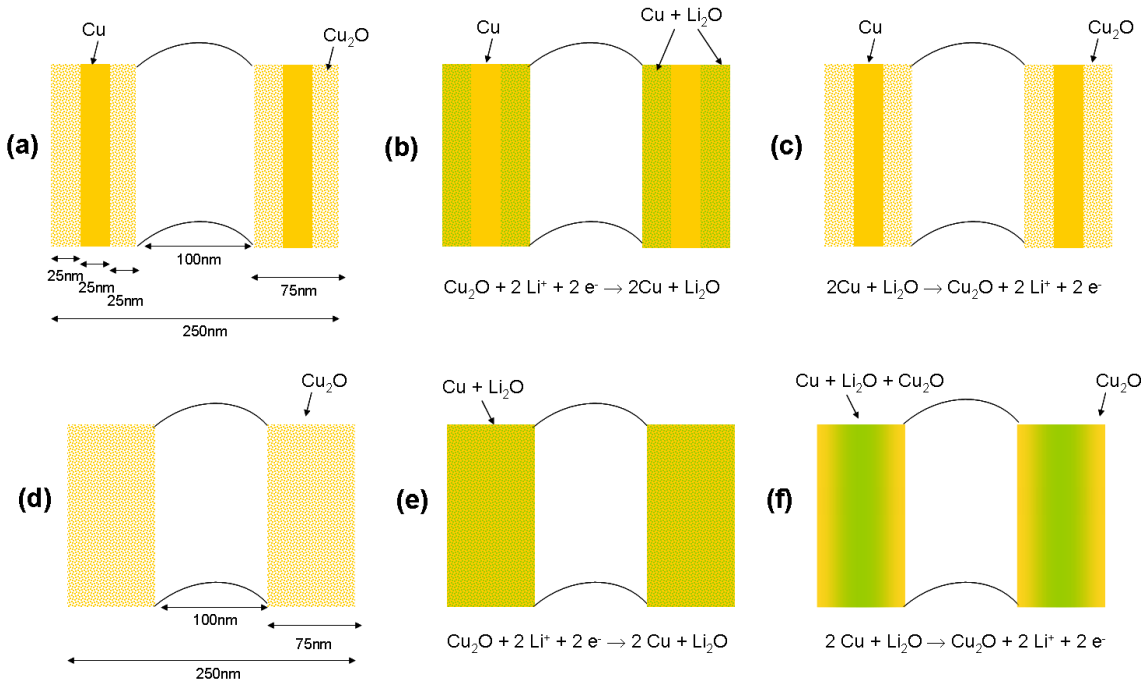

Figure 13. Schematic illustration of the electrochemical conversion reaction of Cu_2O nanotubes (a) Cu_2O outside a Cu core prior to Li^+ insertion, (b) Cu and Li_2O outside Cu core after Li^+ insertion, (c) Restored Cu_2O outside a Cu core after Li^+ extraction, (d) Cu_2O nanotubes without metallic Cu core, (e) Cu and Li_2O after Li^+ insertion, (f) Cu_2O outside isolated Li_2O and discontinuous Cu which cannot support the extraction mechanism due to loss of electrical contact.